

Low frequency plasmons in thin-wire structures

J B Pendry[†], A J Holden[‡], D J Robbins[‡] and W J Stewart[‡]

[†] The Blackett Laboratory, Imperial College, London SW7 2BZ, UK

[‡] GEC-Marconi Materials Technology Ltd, Caswell, Towcester, Northamptonshire NN12 8EQ, UK

Received 16 December 1997, in final form 20 March 1998

Abstract. A photonic structure consisting of an extended 3D network of thin wires is shown to behave like a low density plasma of very heavy charged particles with a plasma frequency in the GHz range. We show that the analogy with metallic behaviour in the visible is rather complete, and the picture is confirmed by three independent investigations: analytic theory, computer simulation and experiments on a model structure. The fact that the wires are thin is crucial to the validity of the picture. This new composite dielectric, which has the property of negative ϵ below the plasma frequency, opens new possibilities for GHz devices.

1. Introduction

This paper is concerned with the electromagnetic response of arrays of thin wires, a typical example of which is shown in figure 1. At one level this structure can be thought of as an array of aerials: a problem for the electrical engineer. We shall show by simple analogy, by detailed computations and by experimental measurements that the plasma resonance in a metal is an accurate paradigm for these thin-wire structures.

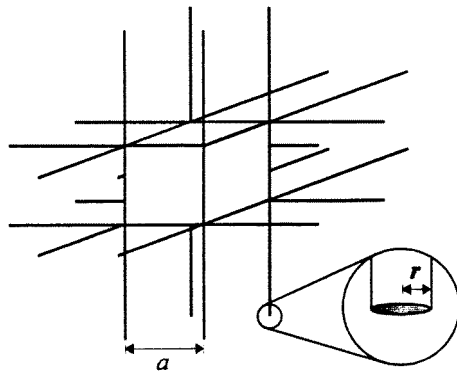


Figure 1. A periodic structure is composed of infinite wires arranged in a simple cubic lattice. In the structures we consider, a might be a few millimetres and r a few microns.

Attention has already been drawn to the singular properties of metallic mesh structures [1, 2]. However to exploit fully the 3D structure of a metallic mesh, radiation must penetrate deep into the structure, something that is difficult to achieve with most metallic structures

whose properties simply reduce to those of a 2D grating. In our earlier paper [2] we pointed out the significance of choosing thin wires, which reduces the interaction of radiation sufficiently to allow penetration and to bring into play the 3D properties of the mesh.

Intense interest has been shown in periodic electromagnetic structures since the demonstration of a photonic band gap by Yablonovitch *et al* [3]: see [4,5] for recent reviews. However most of the attention has been concentrated on dielectric structures. Metallic structures have been considered in a very different context: energy loss in the electron microscope [6–10]. Here it has been known for some time that the structure of metallic objects, such as arrays of colloidal spheres, profoundly affects the loss spectrum. This happens primarily through the metallic surface plasma modes [11,12] which couple very strongly to incident charged particles [13]. If the surfaces are not flat there is also strong coupling to incident transverse modes.

Metals have a characteristic response to electromagnetic radiation due to the plasma resonance of the electron gas [14,15]. Ideally they are described by a dielectric function of the form

$$\varepsilon_{metal} = 1 - \frac{\omega_p^2}{\omega^2} \quad (1)$$

where the plasma frequency, ω_p , is given in terms of the electron density, n , the electron mass, m_e , and charge, e ,

$$\omega_p^2 = \frac{ne^2}{\varepsilon_0 m_e}. \quad (2)$$

Equation (1) implies a dispersion relation shown in figure 2.

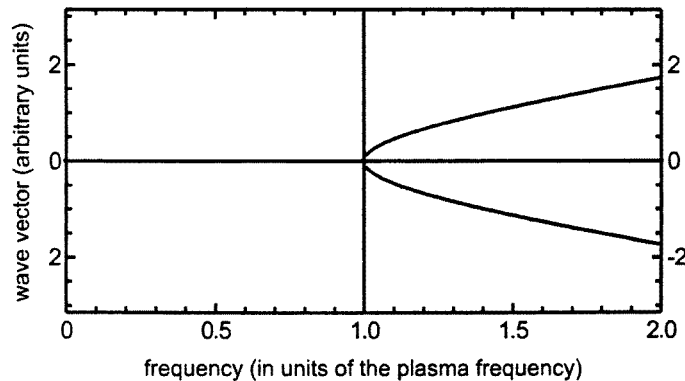


Figure 2. Characteristic dispersion relationship for light in an ideal metal. Two degenerate transverse modes emerge at the plasma frequency and asymptotically approach the free light cone. A singly degenerate longitudinal plasma mode shows no dispersion. Only evanescent modes (imaginary wave vector) exist below the plasma frequency.

A longitudinal mode, the plasmon, appears at a fixed frequency, and two longitudinal modes emerge at the plasma frequency. In consequence of the negative ε , only evanescent modes (imaginary wave vector) exist below the plasma frequency and below this threshold no radiation penetrates very far into the metal. In a normal metal the ideal form is spoiled by the resistance which introduces damping,

$$\varepsilon_{normal} = 1 - \frac{\omega_p^2}{\omega(\omega + i\gamma)}. \quad (3)$$

Typically γ becomes significant in the infra-red. However for a superconductor the condensate continues to display the ideal behaviour and we can, in fact, calculate the London penetration depth from (1).

Much has been made of this dispersion relationship which for the transverse modes is reminiscent of a relativistic massive particle. In particular, Anderson [16] has pointed out that the acquisition of mass, along with the appearance of the dispersionless (i.e. very massive) plasmon, is an example of the Higgs phenomenon. It certainly imparts some unique qualities to metals: their ability to exclude light, the very strong interaction with charged particles, and the curious resonant modes that appear on the surface of a metal in consequence of the negative ϵ below ω_p . The modes may couple to incident radiation provided that the surface is not completely flat, and often give a strong resonant response as in the surface enhanced Raman scattering seen at rough silver surfaces.

Our motivation is to fabricate composite materials that replicate the characteristic features of metallic response to radiation, but in the GHz range of frequencies rather than in the visible. We are particularly interested in the property of negative ϵ , which is not seen in any naturally occurring materials at these frequencies.

We shall first show that a simple analytic argument rapidly develops the plasma analogy. Then we make some more serious calculations by solving Maxwell's equations on a computer and confirming that the simple theory works surprisingly well: quantitative agreement at the 5% level is seen. Next we present experimental data from a thin-wire structure manufactured using spark chamber technology borrowed from high energy physics, and show that this confirms our plasma model with good accuracy, again around the 5% level. Finally, the theory confirmed by experiment, we use the computer to explore variations of the model and show that it is robust under variations in the wire structure: the essential requirements are simply that we have a three dimensional array of thin *continuous* wires.

2. An approximate analytic theory

Before embarking on detailed numerical calculations it is helpful to develop some insight by making an approximate analytical theory. Consider first the response to an electric field applied parallel to one set of wires as shown in figure 3.

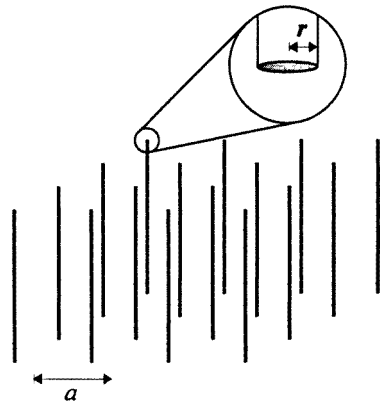


Figure 3. An array of wires aligned with the z axis and arranged on a square lattice in the x - y plane.

Constraining electrons to move along thin wires has two consequences.

The first is that average electron density is reduced because only part of the space is filled by metal,

$$n_{eff} = n \frac{\pi r^2}{a^2} \quad (4)$$

where n is the density of electrons in the wires themselves, r is the radius of the wire and a is the cell side of the square lattice on which the wires are arranged.

The second is an enhancement of the effective mass of the electrons caused by magnetic effects. When any current flows a strong magnetic field is established around the wire given by

$$H(R) = \frac{I}{2\pi R} = \frac{\pi r^2 n v e}{2\pi R} \quad (5)$$

where I is the current flowing in the wire, R is the distance from the wire and v is the mean electron velocity. We can express this field as,

$$\mathbf{H}(R) = \mu_0^{-1} \nabla \times \mathbf{A} \quad (6)$$

where

$$A(R) = \frac{\mu_0 \pi r^2 n v e}{2\pi} \ln(a/R) \quad (7)$$

and a is the lattice constant. We shall justify this formula below.

We note that, from classical mechanics, electrons in a magnetic field have an additional contribution to their momentum of $e\mathbf{A}$, and therefore the momentum per unit length of the wire is

$$e\pi r^2 n A(r) = \frac{\mu_0 e^2 (\pi r^2 n)^2 v}{2\pi} \ln(a/r) = m_{eff} \pi r^2 n v \quad (8)$$

where m_{eff} is the new effective mass of the electrons given by

$$m_{eff} = \frac{\mu_0 e^2 \pi r^2 n}{2\pi} \ln(a/r). \quad (9)$$

Inserting the following values,

$$\begin{aligned} r &= 1.0 \times 10^{-6} \text{ m} & a &= 5 \text{ mm} \\ n &= 1.806 \times 10^{29} \text{ m}^{-3} \text{ (aluminium)} \end{aligned} \quad (10)$$

gives a mass of

$$m_{eff} = 2.4808 \times 10^{-26} \text{ kg} = 2.7233 \times 10^4 m_e = 14.83 m_p \quad (11)$$

where m_e is the electron mass and m_p the proton mass. This is an enormously enhanced effective mass and shifts the plasma frequency by a correspondingly large amount. From the classical formula for the plasma frequency,

$$\omega_p^2 = \frac{n_{eff} e^2}{\epsilon_0 m_{eff}} = \frac{2\pi c_0^2}{a^2 \ln(a/r)} \quad (12)$$

where c_0 is the velocity of light in free space. Substituting gives

$$\omega_p = 5.15 \times 10^{10} \text{ rad s}^{-1} = 8.20 \text{ GHz} \quad (13)$$

in excellent agreement with the computational estimate of 8.3 GHz which we shall make in the next section.

Using equation (12) we can show the importance of thin wires. Supposing that the wires were not thin so that we could neglect $\ln(a/r)$. Then the free space wavelength at the plasma frequency is

$$\lambda_{0p} = 2\pi \frac{c_0}{\omega_p} \approx a\sqrt{2\pi}. \quad (14)$$

In other words without the effect of thin wires λ_{0p} is of the same order as the lattice constant producing diffraction effects which confuse our simple picture. Furthermore if we calculate the penetration depth at, say, half the plasma frequency,

$$\text{penetration depth} = a\sqrt{\frac{2\ln(a/r)}{3\pi}} \quad (15)$$

we can see than without the thin-wire effect radiation hardly penetrates the lattice at all.

Now let us justify the formula quoted for A in equation (7). Suppose that we have a plasmon-like longitudinal excitation in the system shown in figure 3, wave vector parallel to the z axis, with wavelength much longer than the lattice period, a .

$$\mathbf{D} = [0, 0, D_0] \exp[i(kz - \omega t)]. \quad (16)$$

Next we calculate the associated magnetic field from

$$\nabla \times \mathbf{H} = \frac{\partial \mathbf{D}}{\partial t} + \mathbf{j}. \quad (17)$$

Note that if both \mathbf{D} and \mathbf{j} have the same distribution in the x - y plane, then the right-hand side of the above equation vanishes and hence the magnetic field is zero. We can see this by calculating the accompanying charge and current density implied by the longitudinal field,

$$\begin{aligned} \sigma &= \nabla \cdot \mathbf{D} = ikD_0 \exp[i(kz - \omega t)] \\ \mathbf{j} &= i\omega[0, 0, D_0] \exp[i(kz - \omega t)]. \end{aligned} \quad (18)$$

Hence on substituting into (17) the two contributions vanish. This is what happens inside a capacitor discharging through a uniform dielectric filling: no magnetic field is generated.

In our case \mathbf{D} and \mathbf{j} have *different* distributions in the x - y plane. The current is confined to the very thin wires whereas in the limit of long wavelength \mathbf{D} is uniform in the x - y plane. Hence in our case the magnetic field is non-zero and, as we shall show, happens to be large close to the wire. Divide the x - y plane into square unit cells each centred on a wire. On average each cell has zero source with respect to the magnetic field. To calculate the magnetic field we make the approximation of replacing each square cell with a circle of the same area and having a uniform distribution of \mathbf{D} just like the square. The radius of the circle is

$$R_c = a/\sqrt{\pi}. \quad (19)$$

At a given point in the x - y plane the magnetic field only has contributions from the circle inside whose circumference it lies. All other circles have zero contribution. We can easily calculate the magnetic field inside the circle,

$$\begin{aligned} H_c &= \frac{j}{2\pi R} - \frac{j}{2\pi R} \frac{R^2}{R_c^2} & 0 < R < R_c \\ &= 0 & r > R_c \end{aligned} \quad (20)$$

and the corresponding vector potential points along the z axis and has magnitude

$$\begin{aligned} A_c(R) &= \frac{\mu_0 j}{2\pi} \left[\ln\left(\frac{R}{R_c}\right) - \frac{R^2 - R_c^2}{2R_c^2} \right] & 0 < R < R_c \\ &= 0 & R > R_c \end{aligned} \quad (21)$$

where we have exploited our freedom to choose the constant of integration so that \mathbf{A} is zero outside the circle. The point of making this particular choice is that the \mathbf{A} vector of one circle does not overlap with the centre of another and therefore the mutual inductance between the wires has been addressed, at least in this approximation. It only remains to evaluate the \mathbf{A} vector at the wire,

$$A_c(r) = \frac{\mu_0 j}{2\pi} \left[\ln \left(\frac{r}{R_c} \right) - \frac{r^2 - R_c^2}{2R_c^2} \right] = \frac{\mu_0 j}{2\pi} \left[\ln \left(\frac{r\sqrt{\pi}}{a} \right) - \frac{\pi r^2}{2a^2} + \frac{1}{2} \right]. \quad (22)$$

Since in our example,

$$\ln \left(\frac{r}{a} \right) = \ln \left(\frac{10^{-6}}{5 \times 10^{-3}} \right) = -8.5 \quad (23)$$

it is a good approximation to take

$$A_c(r) \approx \frac{\mu_0 j}{2\pi} \ln \left(\frac{r}{a} \right) \quad (24)$$

as we quoted above.

Corrections to the circle approximation are very small because the square cells already have fourfold symmetry and therefore the residual magnetic field will fall off as R^{-4} .

3. Solving Maxwell's equations—numerical simulations

Standard codes exist for the calculation of electromagnetic properties of structured materials [17–19]. They function by dividing space into a mesh of points on which the fields are sampled: typically a uniform mesh is used for simplicity. The problem for thin-wire structures is that a uniform mesh makes an extremely poor sampling of the intense fields near to the wire unless an unacceptably large number of points is used. Otherwise a complex non-uniform mesh needs to be constructed. Fortunately we can avoid both unpleasant alternatives by a simple trick.

The only interest we have in the response of the wires is in the external fields they create far from the wires. Therefore if the thin wires are replaced by thicker wires which have exactly the same external effect, the electromagnetic response will be unaffected. However a thick wire with a relatively uniform distribution of field and current will be much more easily sampled by a uniform mesh than the original thin wire.

3.1. The equivalent conductance of fibres

The objective is to take a wire of small radius in a set of external fields, and replace it with an equivalent fibre of larger radius which has the same external fields (see figure 4). The key quantity will be the current flowing along the length of the wire, J , which we assume to be uniformly distributed over the cross section of the fibre: true if the wire is very thin. This determines the local external magnetic field and therefore must take the same value in both fibres. We calculate the current from the conductance of the wire,

$$J = \pi r_1^2 \sigma_1 E_{1z} \quad (25)$$

$$J = \pi r_2^2 \sigma_2 E_{2z}. \quad (26)$$

E_z has two components: a far-field external component, and a near-field inductive one. First we relate the near field E_z to the magnetic field, then we relate the magnetic field to J and require self-consistency. We start from

$$\nabla \times \mathbf{E} = +i\omega \mathbf{B} \quad (27)$$

and apply Stokes' theorem to the circuit shown in figure 5, giving

$$\oint \mathbf{E}_1 \cdot d\mathbf{l} = i\omega \int_{r_1}^R \mathbf{B}(r) dr. \tag{28}$$

Notice that the contour is everywhere outside the fibre. We shall also assume that there is negligible variation of the relevant fields with z . We can write for the magnetic field, neglecting the displacement current,

$$B_\theta(r) = \frac{\mu_0 J}{2\pi r}. \tag{29}$$

Substituting (29) into (28) gives,

$$E_{1z} = E_0 + i\omega \frac{\mu_0 J}{2\pi} \ln \frac{R}{r_1} \tag{30}$$

where we have required that the asymptotic fields are the same. Substituting into (25) gives

$$J = \pi r_1^2 \sigma_1 E_{1z} = \pi r_1^2 \sigma_1 E_0 + i\omega r_1^2 \sigma_1 \frac{\mu_0 J}{2} \ln \frac{R}{r_1} \tag{31}$$

hence

$$J = \frac{\pi r_1^2 \sigma_1 E_0}{1 - i\frac{1}{2}\omega r_1^2 \sigma_1 \mu_0 \ln(R/r_1)}. \tag{32}$$

Similarly we obtain for the second fibre,

$$J = \frac{\pi r_2^2 \sigma_2 E_0}{1 - i\frac{1}{2}\omega r_2^2 \sigma_2 \mu_0 \ln(R/r_2)}. \tag{33}$$

Inverting (33) we find the equivalent conductance of the second fibre,

$$\sigma_2 = \frac{J}{\pi r_2^2 E_0 + i\frac{1}{2}J\omega r_2^2 \mu_0 \ln(R/r_2)} \tag{34}$$

and substituting from (32) we can express this in terms of the conductance of the original fibre,

$$\sigma_2 = \frac{\sigma_1 (r_1/r_2)^2}{1 - i\frac{1}{2}r_1^2 \sigma_1 \omega \mu_0 \ln(r_2/r_1)} \tag{35}$$

or alternatively we can express this in terms of a dielectric function,

$$\begin{aligned} \epsilon_2 &= 1 + i \frac{\sigma_2}{\omega \epsilon_0} = 1 + i \frac{1}{\omega \epsilon_0} \frac{\sigma_1 (r_1/r_2)^2}{1 + i\frac{1}{2}r_1^2 \sigma_1 \omega \mu_0 \ln(r_1/r_2)} \\ &= 1 + \frac{1}{-i\omega \epsilon_0 \sigma_1^{-1} (r_2/r_1)^2 - \frac{1}{2}r_2^2 \omega^2 c^{-2} \ln(r_2/r_1)}. \end{aligned} \tag{36}$$

Thus we have found a way of replacing the real thin wire with a pseudowire much better suited to computation. In doing so we assumed that the electric field and hence the current was approximately uniform along the wire. This means that effects in which there is local charging of the wire are not accurately reproduced. Also details of the fields near the intersections of wires are not well treated. However we do not anticipate that such details will have any significant consequences.

Fortunately for all transverse waves and for long wavelength longitudinal waves our assumptions are well founded.

As a further precaution the accuracy of the assumptions was checked by repeating numerical calculations for pseudowires of several different radii. If our assumptions are

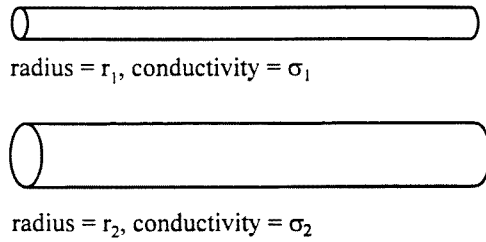


Figure 4. Our objective is to replace the thin wire with an equivalent thick wire which gives the same external responses of the original wire.

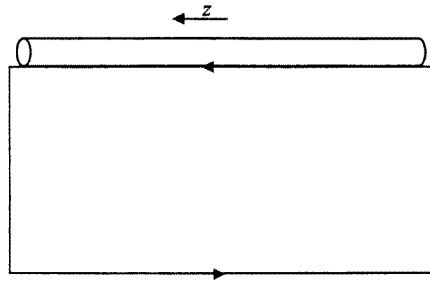


Figure 5. The contour of integration for the electric field is shown: it passes just outside the wire and is closed by a line taken to be far from the wire.

accurate the results should be independent of the pseudowire radius, and this proved to be the case.

We are now in a position to use our standard codes to calculate the properties of a thin-wire lattice and the band structure is shown in figure 6 together with the relevant parameters of the structure. Also plotted in the figure is the analytic estimate of the dispersion relationship obtained in the previous section, though the computed points fall so close to the lines as to obscure them in most instances. As far as the transverse modes are concerned, an effective medium theory with dielectric function as specified above models the data extremely well. The first longitudinal mode is also precisely predicted by the plasmon model. However the ‘second harmonic’ of the plasmon at 15 GHz is not captured by the effective medium, not surprisingly because it is due to trapping of the longitudinal mode travelling in the z direction between consecutive sets of x - y cross wires: a diffraction effect not included in the analytic theory.

4. Experiments on a model structure

4.1. Construction of a negative epsilon material

Thus far our treatment has been entirely theoretical and it is very desirable to confirm the conclusions through experiment, especially as we make radical predictions for the effective dielectric response of the structure. A fully three dimensional structure would be difficult and expensive to manufacture so instead we opted for a simplified version, shown below in figures 7 and 8, that tests all the assumptions made in our theory, but is more amenable to manufacture. A transverse wave incident along the z axis will activate only the x - y wires. The z wires are irrelevant.

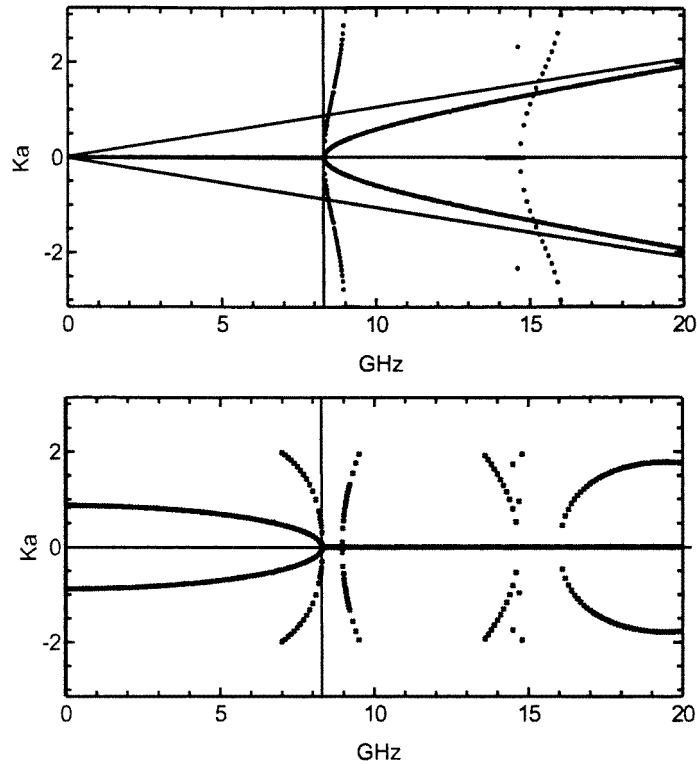


Figure 6. Band structure: real (top) and imaginary (bottom) parts of the wave vector for a simple cubic lattice, $a = 5$ mm, with wires along each axis consisting of ideal metal wires, assumed 1μ in radius. The wave vector is assumed to be directed along one of the cubic axes. The full lines, largely obscured by the data points, represent the ideal dispersion of the longitudinal and transverse modes defined above assuming a plasma frequency of 8.2 GHz. The light cone is drawn in for guidance. Note the two degenerate transverse modes in free space are modified to give two degenerate modes that are real only above the plasma frequency of 8.2 GHz. The new feature in the calculation is the longitudinal mode at the new plasma frequency.

Fortunately for us, thin tungsten wires coated with gold are routinely employed in particle detectors and we were able to persuade the high energy physicists at Imperial College to manufacture the structure for us. It consisted of alternating sheets of 3 mm polystyrene ‘rohacell’ onto which parallel rows of a nominal 20 micron diameter gold plated tungsten wire had been placed with a 5 mm spacing. The sheets were then stacked alternating at right angles to one another resulting in a $5 \text{ mm} \times 5 \text{ mm} \times 6 \text{ mm}$ unit cell and overall dimensions of $200 \text{ mm} \times 200 \text{ mm} \times 120 \text{ mm}$, as shown in figure 9 below. The building blocks are then stacked into a 3D array, alternate layers rotated by 90 degrees. The structure could be dismantled and reassembled with ‘spacer layers’ of blank rohacell added to alter the density of wires and therefore the plasma frequency.

The structure was then handed over to the GEC–Marconi laboratories where measurements were made of the reflection and transmission coefficients.

We expect several characteristic features, particularly in the transmission coefficient:

- Below the plasma frequency epsilon becomes negative and the wave vector imaginary. Hence transmitted intensity falls off exponentially with thickness.

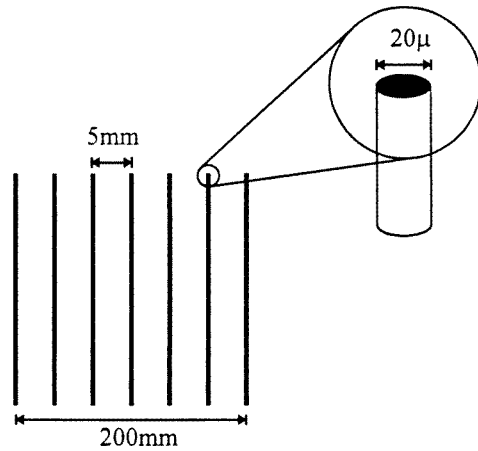


Figure 7. Realization of a negative epsilon structure. Thin gold plated tungsten wires, nominally 20 microns in diameter, are laid in parallel rows onto polystyrene sheets and built into the structure shown above. The aperture is 200 mm \times 200 mm.

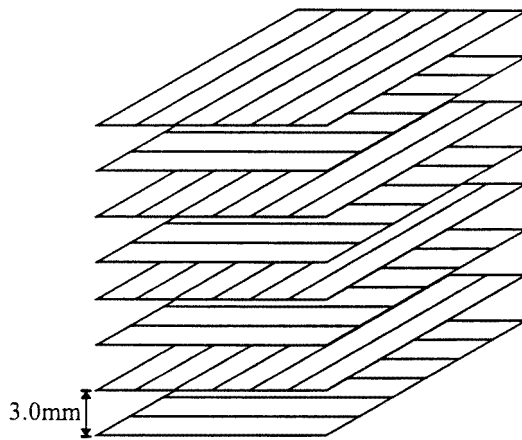


Figure 8. Realization of a negative epsilon structure. Thin gold plated tungsten wires, nominally 20 microns in diameter, are laid in parallel rows onto polystyrene sheets and built into the structure shown above. The aperture is 200 mm \times 200 mm.

- Below the plasma frequency there is no variation of phase as the wave crosses the sample because the wave vector is imaginary.
- Above the plasma frequency the wave vector becomes real and the transmission coefficient grows rapidly to of the order of unity. The rate at which the transmission rises is a measure of how resistive the wires are.
- At the same time the phase starts to vary with frequency in a manner which reveals the underlying dispersion of $k(\omega)$.
- A less pronounced feature in both transmission and reflection coefficients will be the Fabry-Pérot resonances which arise from multiple reflections of the wave within the structure.

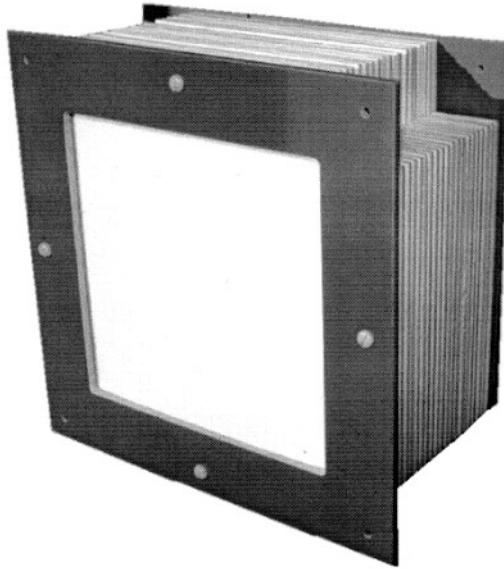


Figure 9. Realization of a negative epsilon structure: photograph of the structure shown in figure 8. The aperture is 200 mm × 200 mm.

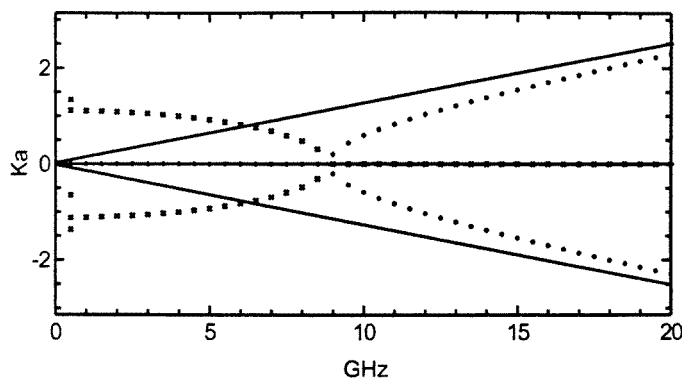


Figure 10. Band structure for the original dense structure, assuming that the wires have zero resistance, and their stated diameter of 20 microns. Real bands: + + +, imaginary bands: × × ×. The full lines show the dispersion of light in free space.

4.2. Measurement on the dense negative epsilon structure

In the first set of measurements the original structure with a dense packing of wires was used. In figure 10 we show the calculated band structure which shows that the plasma edge occurs at approximately 9 GHz; hence we expect a threshold for transmission at this frequency. The experimental data are shown in figure 11.

Next we calculated the transmitted amplitudes for various values of the parameters. The RF resistance of the wires was not available to us so we treated this as a free parameter and, although the wires have a nominal radius of 20 microns, the radius was also used as a parameter. Figure 11 shows the effect of varying the resistance (shown in ohms per metre) and the radius. In general the radius shifts the threshold in frequency, but with a very slow

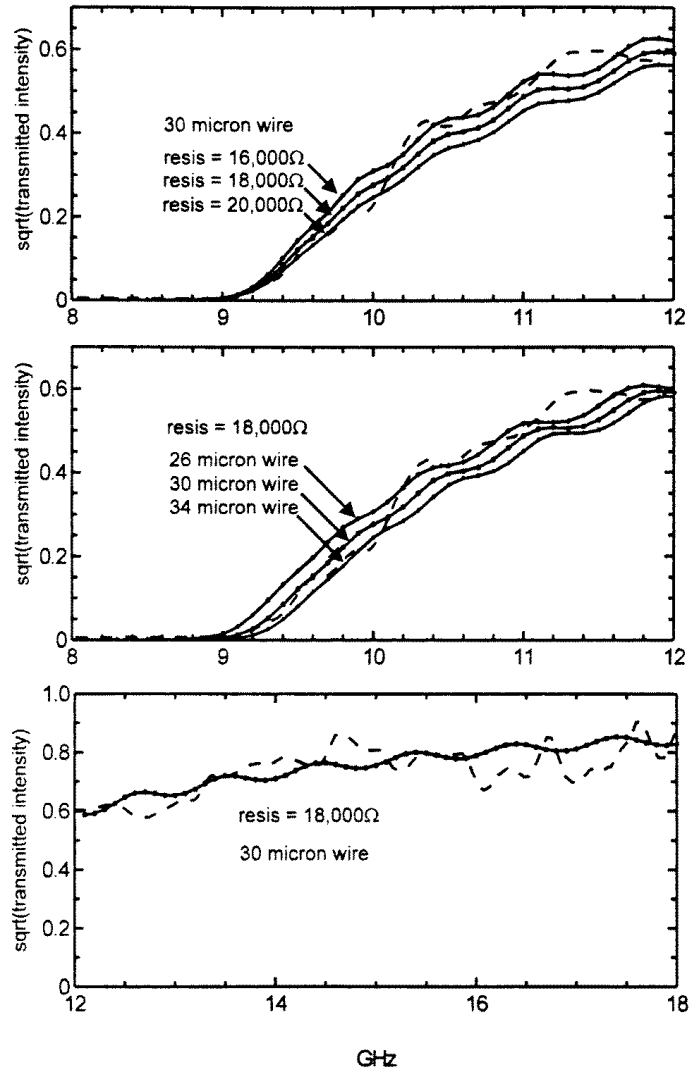


Figure 11. Experimental measurements (dashed curve) of the transmitted amplitude (i.e. square root of the intensity) through 120 mm of a dense photonic wire structure with a $5 \text{ mm} \times 5 \text{ mm} \times 6 \text{ mm}$ unit cell containing two sets of wires at right angles. The full lines in the top figure show three sets of calculations assuming various resistances for the wires, and a diameter of 30 microns. In the middle figure the wire diameter is varied. In the last figure the rest of the frequency range is shown for the optimum parameters.

logarithmic dependence, as can be seen from the lateral shift of the curves. In contrast the resistance controls the amplitude giving a vertical displacement of the curves. The best fit to the radius is about 30 microns, and to the resistance 18 000 ohms. The important conclusion is that the experimental data show the predicted qualitative behaviour, and that the fitted parameters are close to the given ones.

Fine structure observed on the curves is due to multiple reflections inside the sample. Although the experiment does show oscillations they have a shorter period indicating some small stray signals from outside the sample that have a somewhat longer path length.

Having fitted the parameters in the vicinity of the threshold we calculated the transmission coefficient for the higher range of frequencies and compared to experiment. Note that if we ignore the high frequency oscillations due to spurious reflections, the agreement of absolute amplitudes is good.

Next we compared the calculated and measured phases in figure 12. Assuming that most of the contribution to the transmitted amplitude arises from direct transmission through the sample without multiple scattering, the phase will be given by

$$\phi = k(\omega)d \quad (37)$$

where d is the thickness of the sample: 120 mm in this instance. Therefore the phase is a direct measurement of the dispersion relationship $k(\omega)$ to which it is very sensitive because of the relatively large value of d . Below threshold at 9 GHz the phase is not well defined in the experiment, presumably because of spurious reflections. Above threshold agreement is excellent: between 9 and 18 GHz the phase scans through a range of approximately $6 \times 360^\circ$ with an error of around 3%.

4.3. Measurement on the double period negative epsilon structure

Having completed measurements on the dense structure, it was dismantled and reassembled to the same thickness of 120 mm but interspersing each wire sheet with a blank polystyrene sheet. The effect of diluting the wires is to reduce the threshold for transmission as can be seen from the band structure shown in figure 13.

Some numerical instability creeps into the calculations at low frequencies but the key point is the threshold which has now moved down from 9 to 6 GHz as a consequence of the sparser distribution of wires. Additionally we see at higher frequencies around 14 GHz a band gap induced by Bragg scattering from the periodic wire structure. In this frequency range we expect a reduced transmission coefficient details of which can be used further to support our theoretical treatment.

In figure 14 we show the calculated transmitted amplitude. Since we have already determined the wire parameters we should find that the same parameters fit for the double period structure. The previous calculations did not take account of the dielectric constant of the polystyrene sheets. Figure 14 shows that its effect near threshold at 6 GHz is almost completely compensated for by varying the diameter of the wires. However at higher frequencies of 14 GHz, near the band gap where the transmission coefficient takes a dip, the wire diameter is much less important than the dielectric constant.

Comparing calculations to experiment gives a best fit with a diameter of 30 microns as before, and $\epsilon = 1.07$, though the latter parameter is probably only just distinguished from unity. The best fit calculations are compared to experiment in figure 15. The threshold at 6 GHz is very well reproduced. The band gap for the most part is well reproduced. The reduction in intensity at the centre of the gap is confirmation that we have calculated the correct imaginary wave vector which in turn measures the interaction of the wave with the wire structure at these higher frequencies.

One slightly surprising discrepancy is the disagreement between 11 and 12 GHz where experiment shows 10 dB less transmission than the calculation. These frequencies are just below the band gap. There is a less pronounced disagreement just above the band gap. It could be that the RF resistance of the wires is greater than at lower frequencies leading to increased loss in transmission.

Next the transmitted phases were compared in figure 16. Once again, below the threshold at 6 GHz, the phase is ill defined because the transmitted intensity is so small. However from

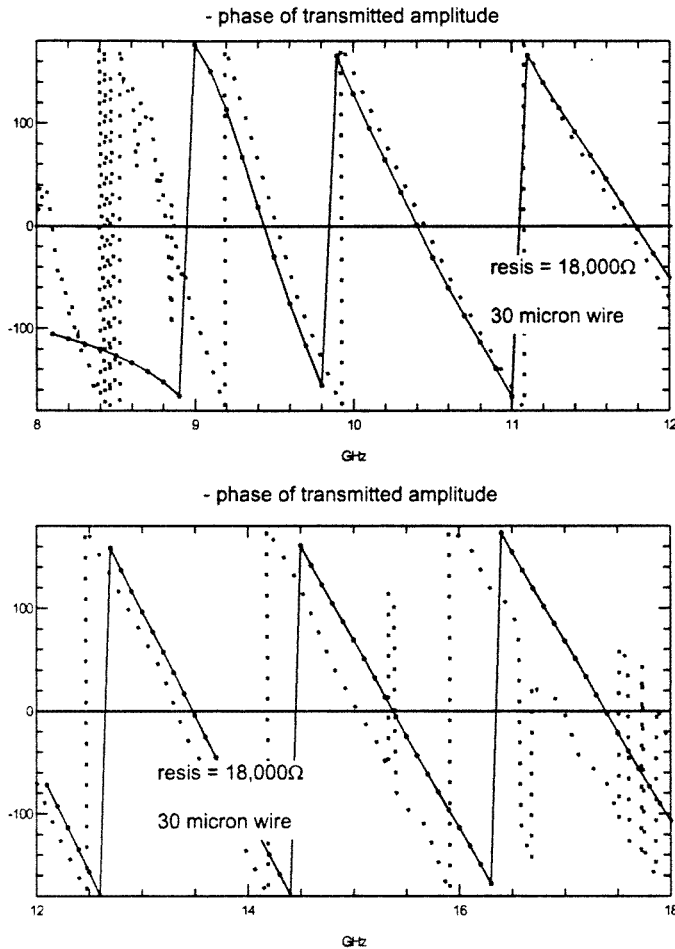


Figure 12. Experimental measurements (dashed curve) of the phase transmitted through 120 mm of a photonic wire structure with a $5 \text{ mm} \times 5 \text{ mm} \times 6 \text{ mm}$ unit cell containing two sets of wires at right angles. The random jumps in phase of π are due to small measurement noise. The full lines show a calculation assuming a resistance of $18000 \text{ ohms m}^{-1}$ for the wires, and a diameter of 30 microns.

the threshold upwards to the beginning of the band gap at 12 GHz there is good agreement. Through the gap itself there is an interesting hiccup which is mostly reproduced, but again the lower side of the gap is a region where agreement is less than perfect indicating the need for some further fine tuning of parameters.

4.4. Conclusions on comparison to experiment

The most important conclusion is confirmation from experiment of the qualitative feature of negative epsilon below a threshold frequency, as evidenced by the cut-off in transmission. In addition we appear to be able to make quantitative predictions for the system, at least at the 5% level of accuracy. The main uncertainty here is the RF resistance of the wire which was fitted to experiment. Independent confirmation of the value used would be helpful

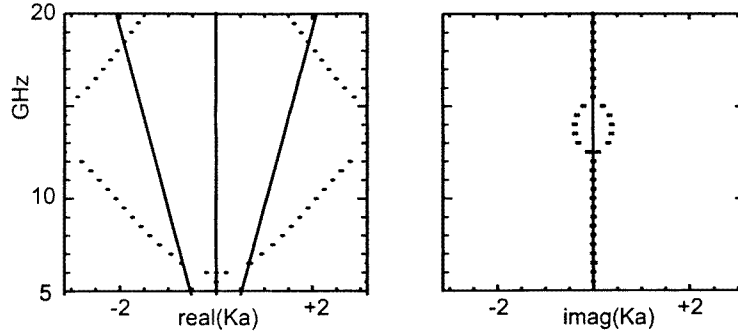


Figure 13. Band structure for the reassembled double period structure with a $5\text{ mm} \times 5\text{ mm} \times 12\text{ mm}$ unit cell containing two sets of wires at right angles, assuming that the wires have zero resistance, and their stated diameter of 20 microns. Left: real bands, right: imaginary bands. The full lines show the dispersion of light in free space. We have ignored numerical instabilities below 5 GHz.

particularly if the frequency dependence could be established. There were some minor discrepancies such as the high frequency oscillations due to multiple scattering processes. In the calculations these were due to multiple passes of the sample, but experiment showed a much shorter period indicating some stray reflections from outside the sample. Theory showed some shortcomings in describing the recovery in transmission coefficient at the lower edge of the band gap.

Overall our theory seems to have good predictive power for these structures.

5. Further tests of the plasmon model

5.1. Does the negative epsilon property depend on direction?

This question is easily answered by extending our earlier calculations for wave vector \mathbf{k} lying along the (001) direction of the simple cubic wire lattice to other directions. Our calculations proceed by fixing ω and k_{\parallel} then finding k_z . We show in figure 17 the trajectory taken by the photon wave vector once k_{\parallel} is fixed.

In a periodic structure the wave vector is defined only within the Brillouin zone. In the case of a simple cubic lattice this consists of a cube centred on the origin extending from

$$\begin{aligned} k_x &= \pm\pi/a \\ k_y &= \pm\pi/a \\ k_z &= \pm\pi/a. \end{aligned} \tag{38}$$

We expect the ideal behaviour defined in the last section to hold only over a limited range of k and ω . However it is desirable that the material should be close to ideal in the vicinity of ω_p and down to as low a frequency as the conductivity of the metal wires permits.

In free space the direction of a wave is defined by

$$k_x, k_y, k_z \tag{39}$$

constrained by

$$k_x^2 + k_y^2 + k_z^2 = \omega^2 c_0^{-2} \tag{40}$$

thus it is possible at a given ω to map out all possible k_x, k_y provided that we are prepared to allow k_z to be imaginary. For example this can be arranged immediately outside a high

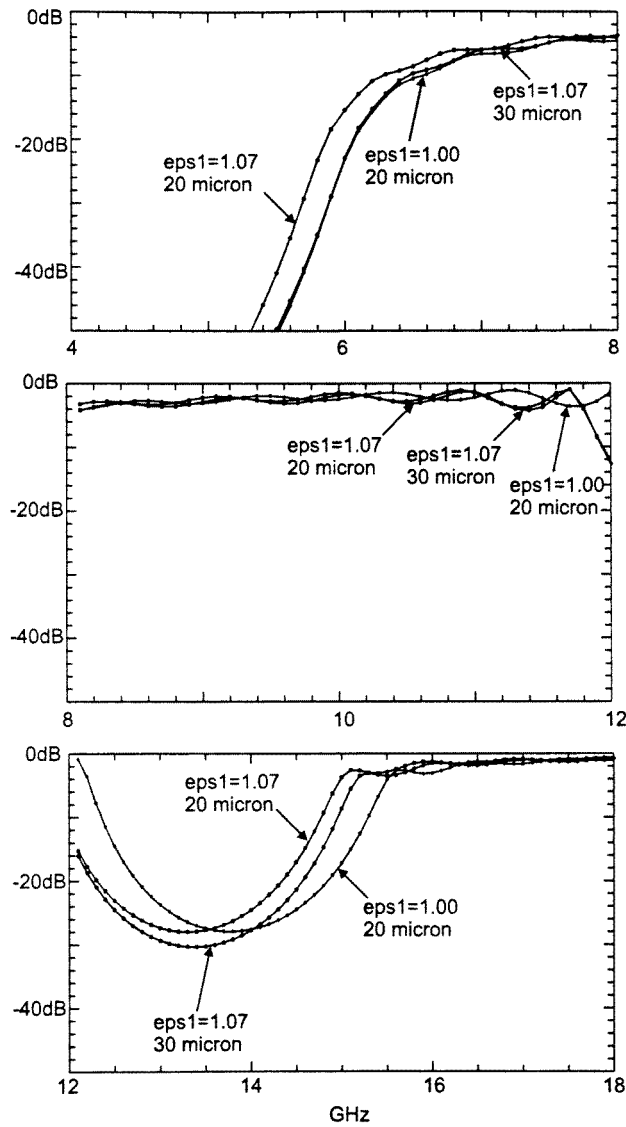


Figure 14. Calculated transmitted amplitude (i.e. square root of the intensity) through 120 mm of a double period photonic wire structure with a $5 \text{ mm} \times 5 \text{ mm} \times 12 \text{ mm}$ unit cell containing two sets of wires at right angles. We assume the same resistance for the wires as used in the dense structure, $18000 \text{ ohms m}^{-1}$. Two diameters are used, 20 microns and 30 microns, and the dielectric constant of the polystyrene host, $\epsilon = 1.07$, is taken into account in two of the calculations.

refractive index material where an evanescent wave may decay strongly into the vacuum. However we suppose that in most practical situations we shall be confined to situations where k_x, k_y, k_z are all real thus limiting the range of values which they make take. In figure 18 we show the range of wave vectors allowed for frequencies up to 20 GHz, approximately twice the plasma frequency, and we shall be content if the ideal model holds within this circle.

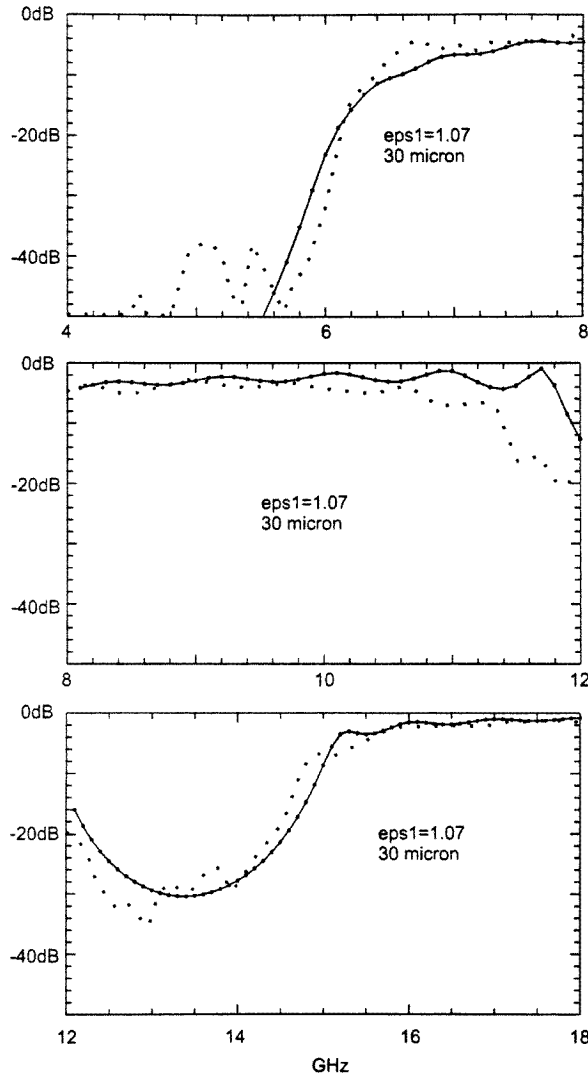


Figure 15. Experimental measurements (dashed curve) of the transmitted amplitude through 120 mm of a double period photonic wire structure with a 5 mm × 5 mm × 12 mm unit cell containing two sets of wires at right angles. The full line shows a calculation in which we assume the same resistance for the wires as used in the dense structure, 18 000 ohms m⁻¹, and a diameter of 30 microns. The dielectric constant of the polystyrene host, $\epsilon = 1.07$, is taken into account in the calculation.

Note that the lattice constant, a , is small compared to a free wave at the plasma frequency. This is because the wires are very thin. In consequence the important range of wave vectors does not reach to the Brillouin zone boundaries which are set by the unit cell dimensions as shown in figure 18.

First we test for wave vectors inside the 20 GHz circle, points A, B, C and D in figure 18, and plot the results in figure 19. We assume a plasma frequency of 8.3 GHz and plot the

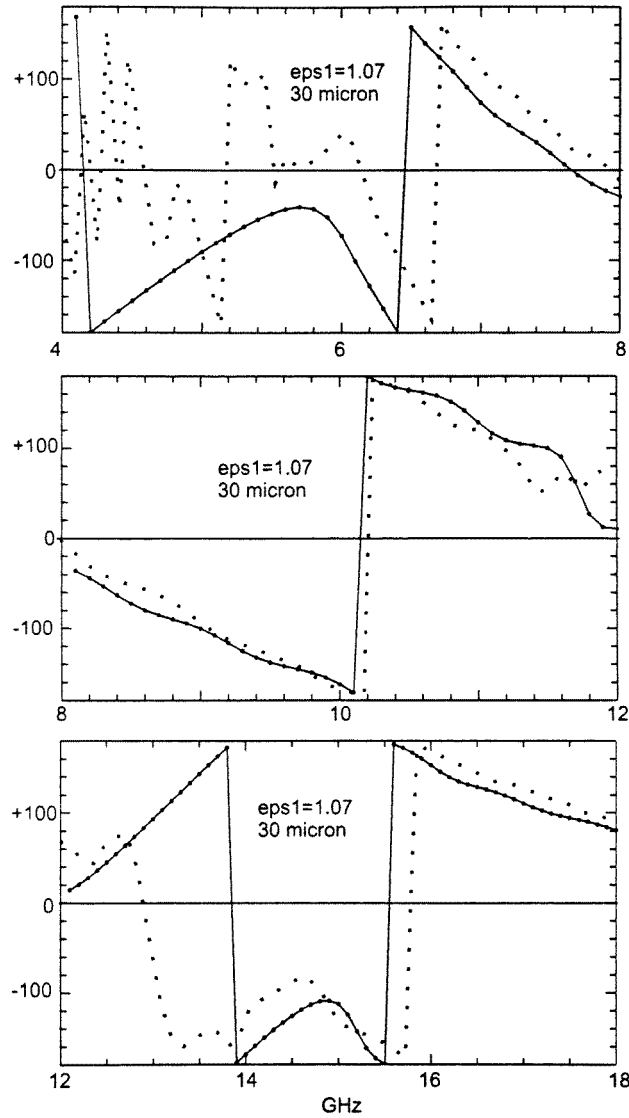


Figure 16. Experimental measurements (dashed curve) of the phase transmitted through 120 mm of a photonic wire structure with a $5 \text{ mm} \times 5 \text{ mm} \times 12 \text{ mm}$ unit cell containing two sets of wires at right angles. The full lines show a calculation assuming a resistance of $18\,000 \text{ ohms m}^{-1}$ for the wires, and a diameter of 30 microns and correspond to the amplitudes shown in figure 15.

dispersion of the longitudinal and transverse modes using this single parameter,

$$\omega^2 = c_0^2 k_x^2 + c_0^2 k_y^2 + c_0^2 k_z^2 + \omega_p^2 \quad (41)$$

and compare with our computations.

Thus in the range of parameters within which we are concerned to test our theory, the computed data fit the model very well: the longitudinal mode is dispersion free to within 10% or 20% indicating that ε is indeed essentially independent of k , and the transverse modes are also well reproduced.

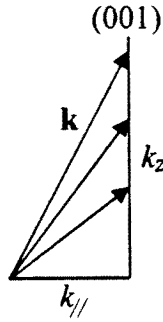


Figure 17. Our programs calculate the band structure, k_z , for fixed ω and $k_{||}$ as shown in this sketch.

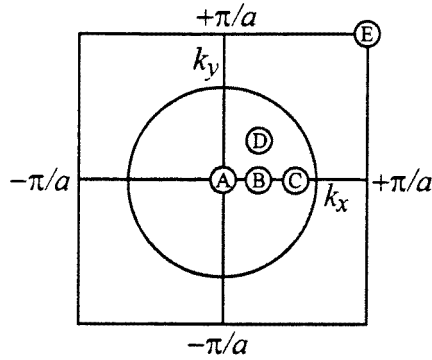


Figure 18. The photon wave vector projected onto the (001) surface Brillouin zone. The circle shows the magnitude of the wave vector for a 20 GHz photon. The band structure in figure 6 is calculated for wave vectors perpendicular to the surface represented by point A in this figure. Other band structure calculations are presented below for non-zero projections of the wave vector onto the surface represented by points B, C, D and E.

As a matter of interest we test a remote point at the farthest corner of the Brillouin zone, point E in figure 18. The results are shown in figure 20.

Clearly when we stray too far out into k space the model breaks down. Nevertheless, even though our calculations are not described by the ideal plasma model, the material still exhibits the negative epsilon property below the plasma frequency and the structure is approximately isotropic in its properties provided that we do not subject the structure to very short wavelength disturbances. It appears that provided that all three wave vectors, k_x , k_y , k_z , are small so that

$$\begin{aligned} \lambda_x &= 2\pi/k_x \gg a \\ \lambda_y &= 2\pi/k_y \gg a \\ \lambda_z &= 2\pi/k_z \gg a \end{aligned} \tag{42}$$

then the ideal model holds good: the photon is too myopic to resolve details of the lattice and sees only an average picture described by an effective local ϵ .

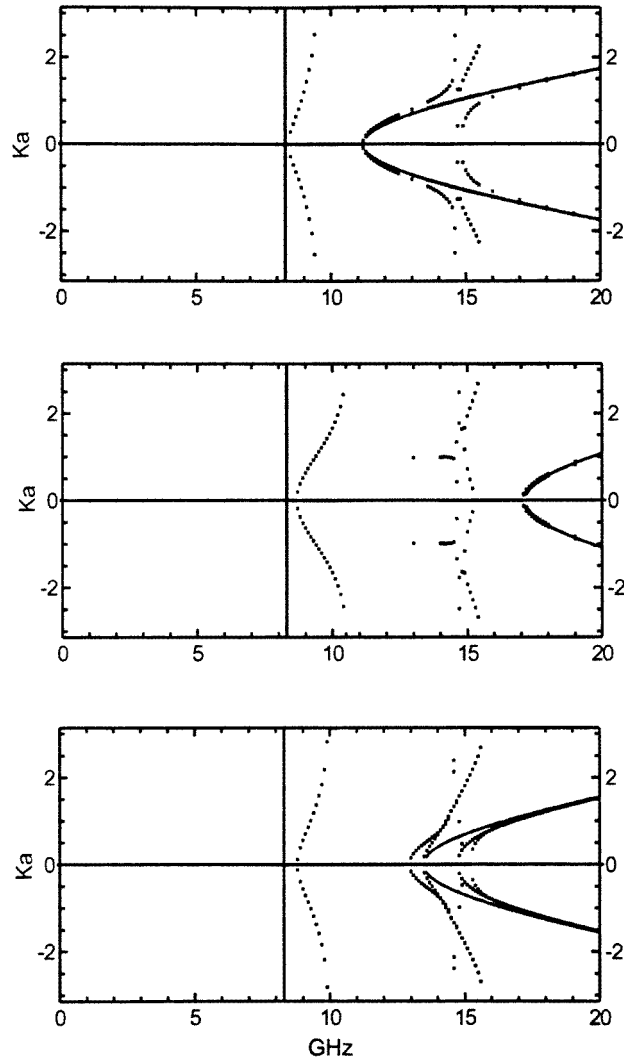


Figure 19. Band structure: real parts of the wave vector for a simple cubic lattice, $a = 5$ mm, with cylinders along each axis consisting of ideal metal fibres, assumed 1μ in radius. The component of the wave vector along the z axis is shown, and the component in the surface plane lies along the x axis with a value shown by points B (top), C (centre), D (bottom) in figure 18. The full lines denote the ideal dispersion relationship expected from equation (41) assuming a plasma frequency of 8.3 GHz.

5.2. Is the detailed arrangement of the wires important?

First we ask how important it is that the three sets of wires touch at the corner of the cells. To answer this question we devised the structure shown in figure 21 where the wires are arranged so as not to touch one another.

The result shown in the second panel of figure 22 is interesting: the transverse modes appear almost exactly the same as in the connected geometry, shown for reference in the top panel, see also figure 6, but the longitudinal mode is very different. The relatively

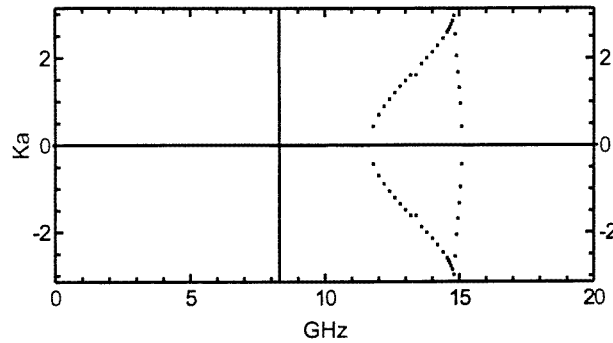


Figure 20. Band structure: real parts of the wave vector for a simple cubic lattice, $a = 5$ nm, with cylinders along each axis consisting of ideal metal fibres, assumed 1μ in radius. The component of the wave vector along the z axis is shown, and the component in the surface plane takes a value $k_x = \pi/a$, $k_y = \pi/a$ (point E in figure 18). Full lines denote the ideal dispersion relationship expected from equation (41) assuming a plasma frequency of 8.3 GHz.

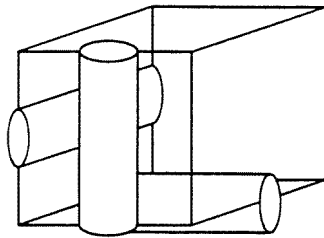


Figure 21. A perspective view of the unit cell for a cubic lattice of non-touching wires. Each wire bisects a side of the unit cell as shown.

high dispersion of the longitudinal mode means that the structure does not fit our ideal model, and in particular ϵ depends on both q and ω which gives difficulties when matching wave functions at the boundary of the material (the additional boundary condition problem). Nevertheless epsilon is undoubtedly negative at low frequencies and this structure merits further investigation.

The most obvious question is whether we need a structure with fibres in all three directions. The answer is almost obvious: transverse modes travelling along the wires will surely see nothing of the wires because their electric fields are perpendicular to them, but longitudinal modes will be strongly affected. Calculations for a single set of wires are shown in the third panel of figure 22.

Note that the transverse modes, the modes which extend down to $\omega = 0$, are almost completely unaffected by the wires and remain free-photon-like, but the longitudinal mode has at $k_z = 0$ exactly the same frequency, 8.3 GHz, as in both the 3D examples, but its dispersion with k_z is strong, resembling that for the 3D structure of unconnected wires, second panel. The transverse wires, when connected to the z wires, appear to play the role of confining dispersion of the longitudinal mode with k_z .

Although not shown in figure 22, the effect of removing wires parallel to the z axis is to leave the transverse modes unaffected, but to remove the plasma mode completely.

We can summarize the effect of removing sets of wires as follows: those modes whose electric fields are parallel to the wires will revert to their free photon format.

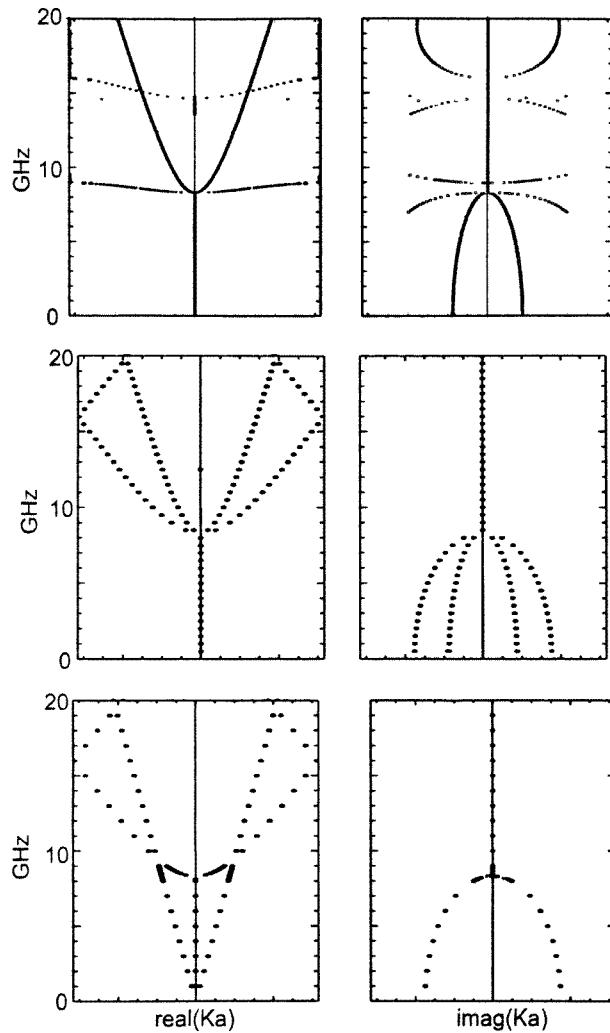


Figure 22. Band structure: left, real part, and right, imaginary part, of the wave vector for a simple cubic lattice, $a = 5$ mm. Top panel: wires along all three axes, intersecting at the corners of the cell (cf figure 6). Middle panel: wires along all three axes but arranged as shown in figure 21 so as not to touch. Bottom panel: wires along only the z axis. The wires are assumed 1μ in radius.

5.3. Is the connectivity of the wires important?

We might suspect that the continuity of the wires is an important attribute: for one thing it ensures a DC conductivity to the structure in the absence of any modes with real wave vector at low frequencies. Let us investigate what happens if we sever the wires: in each unit cell 40% of each of the three wires is cut away. The remaining 60% of the wire is now disconnected from wires in neighbouring cells. The results are shown in figure 23.

The results of cutting the wires into disjointed segments is quite striking: whereas all modes were excluded from low frequencies in the case of continuous wires, now the transverse modes reappear at low frequencies with free-photon-like dispersion reflecting the

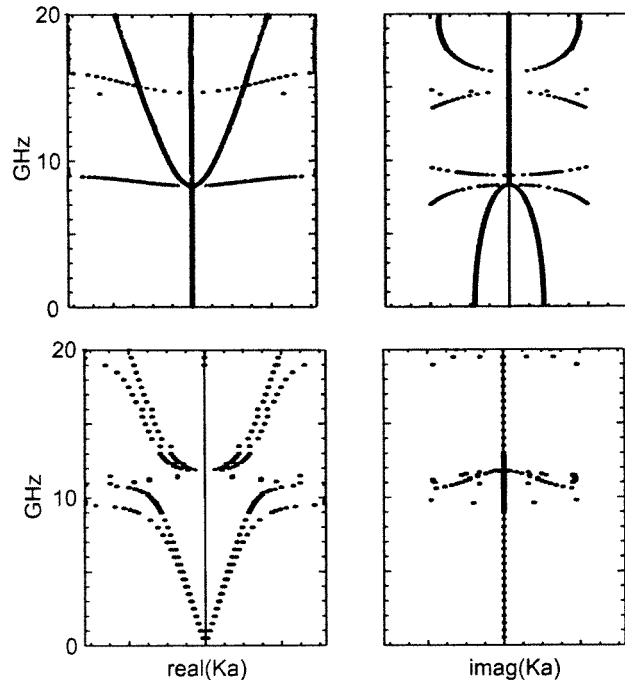


Figure 23. Band structure: left, real part, and right, imaginary part, of the wave vector for a simple cubic lattice, $a = 5$ mm. Top panel: wires along all three axes, intersecting at the corners of the cell (cf figure 6); bottom panel: as above but the cylinders are cut into segments occupying 60% of the cell length. The wires are assumed 1μ in radius.

fact that the material is effectively an insulator in the low frequency regime. A longitudinal mode still exists close to the old plasma frequency but can hardly be interpreted as a plasma mode because its controlling influence on the transverse modes has disappeared. In fact the results look more like those for a system of interacting dipoles [20].

We conclude that continuity of the wires is vital to observing the plasma-like behaviour. Severance of the wires immediately results in reappearance of transverse modes at low frequencies and vanishing of the ‘negative epsilon’ property. Other changes to the structure have less severe consequences. We have experimented with structures into which extra lengths of wire have been introduced, for example the structure shown in figure 24. Calculations show that, provided the connectivity of the wires is maintained, the structure continues to behave like a plasma, but the plasma frequency is lowered by the extra inductance of the greater length of wire.

6. Conclusions

We have made a thorough investigation of the properties of structures made from 3D arrays of continuous thin wires and shown that the properties of such structures are well described by a plasma model. The structures are characterized by a plasma frequency below which all modes decay exponentially, and above which transverse modes propagate like massive particles. At the plasma frequency there is a longitudinal mode. These properties were established by analytical modelling (which proved surprisingly accurate), numerical solution of Maxwell’s equations and finally by experimental investigation.

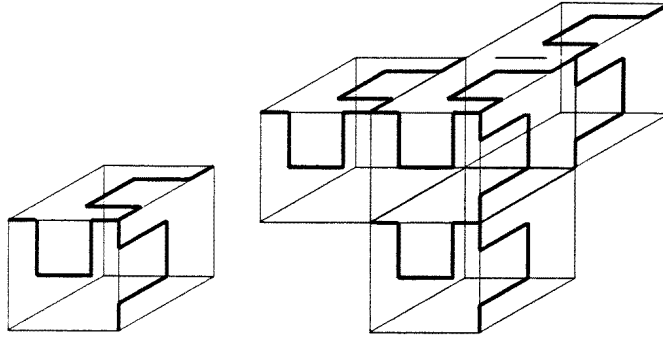


Figure 24. A connected bent wire structure showing the unit cell on the left, and four neighbouring cells on the right. The wires are connected at the cell vertices.

The wires had to be continuous and, unless they were thin, the fields penetrated no more than one layer below the plasma frequency. Using thin wires also reduced the plasma frequency so that externally incident waves at this frequency had too long a wavelength to be diffracted. This meant that the system could be accurately described by an effective dielectric constant of the plasma form.

Having established this principle we now have a playground for creating novel systems. Material with these dielectric properties will couple very strongly to electrical charge and will be efficient at extracting energy as a form of Čerenkov radiation into the slow travelling modes near the plasma frequency. Further, the plasma mode can be further tailored by the external structure of the composite. For example, the surface of such a composite will be host to a surface plasma mode at

$$\omega_s = \omega_p / \sqrt{2}. \quad (43)$$

Although our prime interest in these structures is to develop novel composite materials for microwave applications, there are other possibilities raised by the structure. The connection to superconductivity has been alluded to: in particular the negative epsilon property will survive down to DC frequencies if the wires are made from superconducting material. This raises the intriguing observation that we now can manufacture a composite superconducting material in which the plasma energy, $\hbar\omega_p$, is of the same order as the pairing energy, Δ . In conventional superconductors the plasma frequency is much too high to play any direct role in pairing, but could our new composite change this?

The material has an extremely simple internal structure and employs only minute amounts of metal: structures consisting of parts per million of metal can be active in the microwave region. This presents us with many opportunities for design.

Acknowledgments

We thank Derek Miller and Dave Clark, of the High Energy Physics group at Imperial College, who were responsible for constructing our model negative epsilon structure, also Les Hill of GEC–Marconi Materials Technology Ltd who measured the response of the model. This work has been carried out with the support of the Defence Research Agency, Holton Heath.

References

- [1] Sievenpiper D F, Sickmiller M E and Yablonovitch E 1996 *Phys. Rev. Lett.* **76** 2480
- [2] Pendry J B, Holden A J, Stewart W J and Youngs I 1996 *Phys. Rev. Lett.* **76** 4773
- [3] Yablonovitch E, Gmitter T J and Leung K M 1991 *Phys. Rev. Lett.* **67** 2295
- [4] Yablonovitch E 1993 *J. Phys.: Condens. Matter* **5** 2443
- [5] Pendry J B 1996 *J. Phys.: Condens. Matter* **8** 1085
- [6] Ritchie R H and Howie A 1981 *Phil. Mag. A* **44** 931
- [7] Echenique P M and Pendry J B 1975 *J. Phys. C: Solid State Phys.* **8** 2936
- [8] Ferrell T L and Echenique P M 1985 *Phys. Rev. Lett.* **55** 1526
- [9] Echenique P M, Howie A and Wheatley D J 1987 *Phil. Mag. B* **56** 335
- [10] Howie A and Walsh C A 1991 *Microsc. Microanal. Microstruct.* **2** 171
- [11] Ritchie R H 1957 *Phys. Rev.* **106** 874
- [12] Stern E A and Ferrell R A 1960 *Phys. Rev.* **120** 130
- [13] Pendry J B and Martín Moreno L 1994 *Phys. Rev. B* **50** 5062
- [14] Pines D and Bohm D 1952 *Phys. Rev.* **85** 338
- [15] Bohm D and Pines D 1953 *Phys. Rev.* **92** 609
- [16] Anderson P W 1963 *Phys. Rev.* **130** 439
- [17] Pendry J B and MacKinnon A 1992 *Phys. Rev. Lett.* **69** 2772
- [18] Pendry J B and MacKinnon A 1993 *J. Mod. Opt.* **41** 209
- [19] Bell P M, Pendry J B, Martín Moreno L and Ward A J 1995 *Comput. Phys. Commun.* **85** 306
- [20] van Coevorden D V, Sprik R, Tip A and Legendijk A 1996 *Phys. Rev. Lett.* **77** 2412